

Article

Copper-Tin Alloys for the Electrocatalytic Reduction of CO₂ in an Imidazolium-Based Non-Aqueous Electrolyte

Robert L. Sacci ^{1,*}, Stephanie Velardo ², Lu Xiong ², Daniel A. Lutterman ^{1,*,†} and Joel Rosenthal ^{2,*} 

¹ Chemical Sciences Division, Oak Ridge National Laboratory, Oak Ridge, TN 37831, USA

² Department of Chemistry and Biochemistry, University of Delaware, Newark, DE 19716, USA

* Correspondence: saccirl@ornl.gov (R.L.S.); daniel.lutterman@knoxvillecatholic.com (D.A.L.); joelr@udel.edu (J.R.)

† Knoxville Catholic High School, 9245 Fox Lonas Rd NW, Knoxville, TN 37923, USA.

Received: 12 June 2019; Accepted: 7 August 2019; Published: 15 August 2019

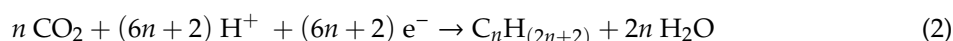


Abstract: The ability to synthesize value-added chemicals directly from CO₂ will be an important technological advancement for future generations. Using solar energy to drive thermodynamically uphill electrochemical reactions allows for near carbon-neutral processes that can convert CO₂ into energy-rich carbon-based fuels. Here, we report on the use of inexpensive CuSn alloys to convert CO₂ into CO in an acetonitrile/imidazolium-based electrolyte. Synergistic interactions between the CuSn catalyst and the imidazolium cation enables the electrocatalytic conversion of CO₂ into CO at −1.65 V versus the standard calomel electrode (SCE). This catalyst system is characterized by overpotentials for CO₂ reduction that are similar to more expensive Au- and Ag-based catalysts, and also shows that the efficacy of the CO₂ reduction reaction can be tuned by varying the CuSn ratio.

Keywords: electrocatalysis; electrodeposition; CO₂ electroreduction; non-aqueous electrolytes

1. Introduction

The development of cost-effective systems for the conversion of CO₂ into value-added products and high-energy species such as CO and saturated hydrocarbons is of global importance [1,2]. In 2016, industrial, commercial, and private transportation alone generated over 5000 metric tons of atmospheric CO₂ through the burning of fossil fuels [3]. Together with other CO₂ emitting processes, fossil fuel combustion continues to drive climate change and exacerbates the natural greenhouse effect [4]. Without improved energy harvesting, storage, and CO₂ sequestration technologies, this trend will only continue to increase [5]. Renewable electric energy sources such as solar or wind harvesting technologies can be utilized to power thermodynamically uphill energy storing electrochemical reactions [1,2,5]. Historically, coinage metals (Au, Ag, and Cu) have been utilized as electrocatalysts for the reduction of CO₂ to CO and saturated hydrocarbons (methane, ethane, propane, etc.) via Equations (1) and (2), respectively [6,7].



Electrolysis using copper cathodes can also promote the conversion of CO₂ into simple alcohols (i.e., methanol, ethanol, propanol, etc.) via the balanced process shown in Equation (3). In addition to the direct reduction of CO₂ to hydrocarbons and oxygenates, a secondary process that converts H₂O into H₂ can be used in conjunction with the electrocatalytic CO production to produce syngas

(a CO/H₂ mixture), which is a primary feedstock that can be unconverted into liquid carbon-based fuels such as gasoline and diesel via Fischer-Tropsch processes [8].

It has been shown that the $2e^-/2H^+$ CO₂ reduction reaction (CO₂RR) to generate CO is promoted by metallic cathodes in the presence of imidazolium-based ([Im]⁺) non-aqueous electrolytes [9–13]. The [Im]⁺ cation is believed to serve as a proton donor and also acts to stabilize reduced CO₂ intermediates that are formed/adsorbed at the cathode/electrolyte interface [14], while promoting proton and electron transfer processes attendant to CO₂ reduction [15]. In fact, CO₂ electroreduction in [Im]⁺-based electrolytes has been shown to occur *selectively* and *efficiently* using inexpensive non-noble cathodes such as bismuth [16,17]. These metals inhibit the kinetics for the H₂ evolution reaction (HER) by increasing the activation energy of the surface hydride formation [18,19]. In this manner, H₂ Faradaic efficiency (FE) is dramatically suppressed (FE_{H₂} < 2%), allowing the CO₂RR reactivity to dominate on Bi [13,17,20]. Sn represents another post-transition metal that has been shown to facilitate the CO₂RR in [Im]⁺-based electrolytes, although with a slightly higher overpotential than Bi [16].

In many systems, bimetallic and alloy catalysts have shown improvements over their base components for electrocatalysis applications. Since, as mentioned above, Sn has been shown to facilitate the CO₂ reduction reaction (CO₂RR) to generate CO from CO₂ dissolved in [Im]⁺/MeCN-based electrolytes ($j \sim 7.5$ mA/cm at -1.95 V vs. SCE), we considered the ability of Sn-containing alloys to promote the CO₂RR under similar conditions. In this study, we present the use of Cu₆Sn₅ and Cu₆Sn₁₀ thin film alloys as electrocatalysts for the CO₂RR in [Im]⁺/MeCN-based electrolytes. This work complements recent studies by Haruyama and coworkers, which demonstrated that electrodeposited CuSn alloys can promote the reduction of CO₂ to both CO and formate in aqueous electrolytes that do not contain [Im]⁺ promoters [21]. These authors reported that the selectivity of formate production was enhanced with increased Sn stoichiometry in the film. In this work, we compare the activity and selectivity of a pure phase CuSn alloy with one having excess Sn, and document the CO₂RR performance of these systems in MeCN containing [BMIM]⁺ electrolytes.

2. Experimental

Reagents, solvents, and all other chemicals were purchased from Fisher, Alfa Aesar, TCI America, Sigma-Aldrich, Acros Organics, Matrix Scientific, or Cambridge Isotopes Laboratories. Electrochemical grade tetrabutylammonium hexafluorophosphate (TBAPF₆) was obtained from TCI America and was purified by recrystallization from ethanol prior to use. Compressed carbon dioxide gas was supplied by Keen Compressed Gas Company.

Cu₆Sn₅ and Cu₆Sn₁₀ targets were prepared from stoichiometric mixtures of Sn (99.8%, Alfa Aesar, Haverhill, MA, USA) and Cu (99.5%, Sigma-Aldrich, St. Louis, MO, USA) that were ball milled with yttria-stabilized zirconia balls for 15 min. This powder was then pressed into a 50 mm diameter disk, annealed at 200 °C under Ar, and slowly cooled to ambient temperature. The Cu₆Sn₅ target was analyzed by X-ray diffraction (XRD) and was shown to correspond to the expected η -Cu₆Sn₅ (C2/c) monoclinic phase formed at low temperatures with lattice parameters $a = 11.0262 (\pm 0.0014)$ Å, $b = 7.2745 (\pm 0.0012)$ Å, and $c = 9.846 (\pm 0.0021)$ Å [22]. The Cu₆Sn₁₀ target was a mixture of Sn and the Cu₆Sn₅ monoclinic phase.

Thin film depositions were carried out using direct current (DC) magnetron sputtering of the above alloyed targets in argon plasma onto (2000-grit) polished nickel foils. Sputtering was conducted at 10 W, 20 mTorr, and with a 5 cm target–substrate distance. This resulted in a deposition rate of about 0.9 nm s⁻¹ and yielded thin films with the structure of the high temperature hexagonal Cu₆Sn₅ ($P6_3/mmc$, ICDD 00-002-0713) phase [22] and Cu₆Sn₁₀ was a mixture of Sn ($I4/mmm$, ICDD 96-900-8571) and the η -Cu₆Sn₅ phase (see Results and Discussion). Film thicknesses were systematically varied between 0.1 and 0.5 mm.

2.1. Film Characterization

A Scintag PDS 2000 diffractometer equipped with Cu-K α radiation and a nickel filter were used for XRD collection. Scattering angles of 10–100° were collected in 0.02°-steps with a count time of 5 s per step.

Rietveld refinements were performed using the PANalytical HighScore Plus software (3.5, PANalytical B.V., Almelo, The Netherlands) package by indexing with powder diffraction files (ICDD and COD).

Scanning electron microscopy (SEM) images and energy dispersive X-ray (EDX) spectra were obtained using a JEOL JSM 7400F Scanning Electron Microscope. X-ray photoelectron spectroscopy (XPS) experiments were carried out using a VG ESCALAB 220I-XL spectrometer equipped with a non-monochromatic Al K_{α} source operating at 300 W. Initial XPS survey scans were collected at a pass energy of 100 eV using a step size of 1.0 eV. All high-resolution XPS spectra were recorded at a pass energy of 20 eV using a step size of 0.1 eV. Atomic ratios were determined using a Shirley-type baseline and standard relative sensitivity factors. Additional XPS characterization of the sputtered films was carried out using a PHI 3056 spectrometer with a non-monochromatic Mg K_{α} source operated at 15 kV and 350 W. Through comparison with the adventitious C 1s signal, the XPS spectra in Figure 1 will show a 0.9 eV shift to lower binding energies.

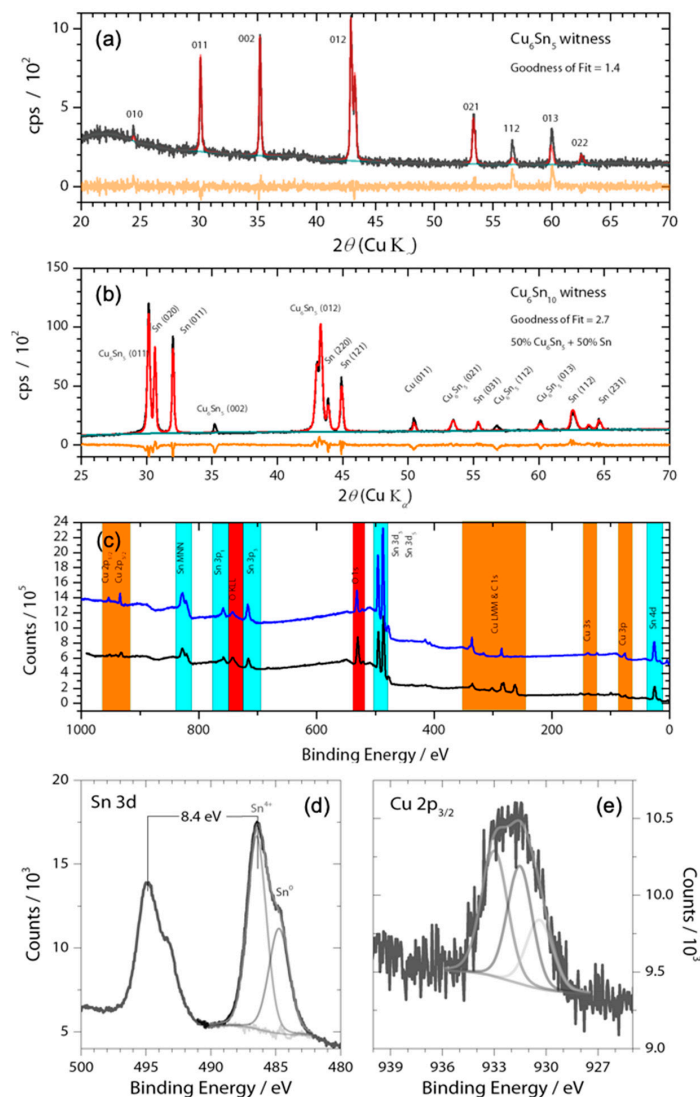


Figure 1. (a,b) X-ray diffractogram of witness Cu_6Sn_5 and $\text{Cu}_6\text{Sn}_{10}$ thin films along with Rietveld refinement using Highscore Plus and ICDD; black lines are raw data, red lines are the fit data, and orange lines the residual; (c) Survey XPS (Mg source) spectrum of the thin films on nickel foil current collectors showing photoelectron emissions from only O, adventitious C, Cu, Sn, and Ni substrate. High resolution XPS spectra of (d) Sn 3d and (e) Cu $2p_{3/2}$ along with peak fittings highlights the presence of oxides within the Cu_5Sn_6 film. Note: Sn^{2+} may also be present in the Sn 3d XPS spectrum, as Sn^{4+} and Sn^{2+} have similar binding energies that differ by only ~ 0.6 eV. No corrections to binding energy were made.

2.2. Electrochemistry

All electrochemistry was performed using either a CHI-620D potentiostat/galvanostat or a CHI-720D bipotentiostat. Cyclic voltammetry (CV) and linear-sweep voltammetry (LSV) experiments were carried out using standard three-electrode configurations. A section of platinum gauze (Sigma 99.9%) served as the auxiliary electrode, and was separated from the working and reference electrodes by Nafion membranes. All potentials were measured against a Ag/AgCl reference electrode (1.0 M KCl, CH Instruments) and were converted into SCE ($E_{SCE} = E_{Ag/AgCl} + 44 \text{ mV}$). Cyclic voltammograms were recorded at 100 mV/s and were IR compensated. Unless otherwise noted, 0.1 M tetrabutylammonium hexafluorophosphate (TBAPF₆) in MeCN was used as the supporting electrolyte for all electrochemical studies. The MeCN utilized for electrochemical experiments was not rigorously dried and contained adventitious levels of moisture.

Controlled potential electrolysis (CPE) experiments were performed in gas-tight two-compartment cells with a Nafion (NRE-212) membrane separating the anode and cathode compartments, as has been previously described [17]. Both the cathode and anode compartments of the electrolysis cell were filled with 20.0 mL of 0.1 M tetrabutylammonium hexafluorophosphate (TBAPF₆) in MeCN, and were bubbled with CO₂, Ar, or N₂ for at least 30 min prior to performing the electrochemical experiments.

During all CPE experiments, the cathode solution was stirred vigorously while a constant supply of MeCN-saturated CO₂ gas was fed into the headspace of the electrolysis cell at a rate of 5.0 cm³/min. The cathode compartment was vented into an autosampling loop of a gas chromatograph (GC) (SRI Instruments, SRI-8610C). GC acquisitions were initiated every 15 min by placing the autosampling loop in line with a packed HayeSep D column and a packed MoleSieve 13× column. Argon (Keen, 99.999%) was used as the GC carrier gas. Both GC columns connected directly to a thermal conductivity detector (TCD) to quantify hydrogen and a flame ionization detector (FID) equipped with a methanizer unit to quantify the production of reduced carbon species such as carbon monoxide. The partial current densities associated with electrolytic formation of CO and H₂ were calculated from the GC peak area as follows:

$$j_{\text{CO}} = \frac{\text{Peak Area}}{\alpha} \times \text{Flow Rate} \times \frac{2Fp_0}{RT} \times (\text{Electrode Area})^{-1}$$

$$j_{\text{H}_2} = \frac{\text{Peak Area}}{\beta} \times \text{Flow Rate} \times \frac{2Fp_0}{RT} \times (\text{Electrode Area})^{-1}$$

In the above two equations, α and β represent conversion factors based on the calibration of the GC with standard samples of CO and H₂, respectively, $F = 9.65 \times 10^4 \text{ C mol}^{-1}$, $p_0 = 1 \text{ atm}$, $R = 82.1 \text{ mL atm K}^{-1} \text{ mol}^{-1}$, and $T = 298 \text{ K}$. Faradaic efficiencies for the formation of a given product were calculated by dividing the partial current densities by the total current. ¹H NMR experiments were performed on aliquots of the electrolyte solution at the completion of each electrolysis run to determine whether nonvolatile CO₂RR products had formed, and to monitor changes to the composition of the electrolyte solution. NMR spectra were recorded at 25 °C on a Bruker 600 MHz NMR spectrometer.

3. Results and Discussion

3.1. Catalyst Characterization

The CuSn alloys were deposited from Cu₆Sn₅ or Cu₆Sn₁₀ targets onto nickel foils. X-ray diffraction experiments showed that the thin film generated by sputtering the Cu₆Sn₅ target belonged to the *P6₃/mmc* space group (Figure 1a), which is indicative of hexagonal η -Cu₆Sn₅. By contrast, the thin film generated by sputtering the Cu₆Sn₁₀ target was shown to be a mixture of η -Cu₆Sn₅ and pure Sn phases. Given that thin films typically have a preferred orientation, the refinement of the diffraction pattern was kept qualitative for phase identification. The stoichiometry of these deposits was confirmed by XPS analysis (Figure 1); however, these experiments also showed evidence of the presence of a native Sn-oxide layer (Figure 1c,d) on the film surface that was at least 2-nm thick. The Cu 2p_{3/2} peak appears to be composed of three species. There appears to be Cu₂O and CuO given the signal at 933.2 and

930.5 eV, respectively [23]. The Cu 2p_{3/2} peak in Cu₆Sn₅ has been found to be around 932.6 eV [24], which agrees with our value of 931.6 eV (recall 0.9 eV offset). The sputtering produced a rough and polycrystalline surface with sub-micron grains, as demonstrated by the SEM images shown in Figure 2. The presence of a pure Sn phase in Cu₆Sn₁₀ qualitatively appears to decrease the average particle size of this sputtered film, as evidenced by the SEM images of Figure 2.

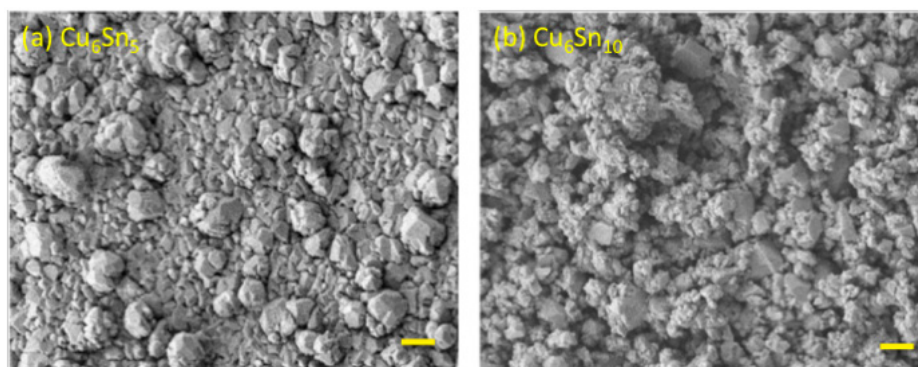


Figure 2. Scanning electron micrograph (SEM) images recorded for evaporated thin films of (a) Cu₆Sn₅ and (b) Cu₆Sn₁₀. The scale bars correspond to a length of 1.0 μm.

3.2. Catalyst Activity

Figure 3a shows linear sweep voltammograms recorded for the CuSn alloys submerged in electrolyte solutions containing 0.1M TBAPF₆ and 70 mM of the ionic liquid (IL) additive [BMIM]OTf, under an atmosphere of either N₂ or CO₂. Notably, no current response is observed for either CuSn film in the absence of CO₂, consistent with the voltammetric response being correlated with CO₂RR activity. Panels (b) and (c) of Figure 3 demonstrate the effect of varying the concentration of [BMIM]OTf on the CO₂RR activity of both CuSn alloys. Notably, in the absence of the [BMIM]⁺-based IL, no CO₂ activation takes place, indicating that the [Im]⁺ cation is critical to the observed CO₂RR and voltammetric responses. The addition of [BMIM]OTf to the CO₂-saturated solution clearly shows CO₂RR activity with an onset potential of $E \sim -1.65$ V vs. SCE for both the Cu₆Sn₅ and Cu₆Sn₁₀ films, but *only* in the presence of CO₂ (Figure 3a). The need for both CO₂ and [BMIM]⁺ to observe the current responses of Figure 3 is consistent with the imidazolium-assisted activation of CO₂ by the CuSn films, as opposed to direct [BMIM]⁺ reduction [13,20].

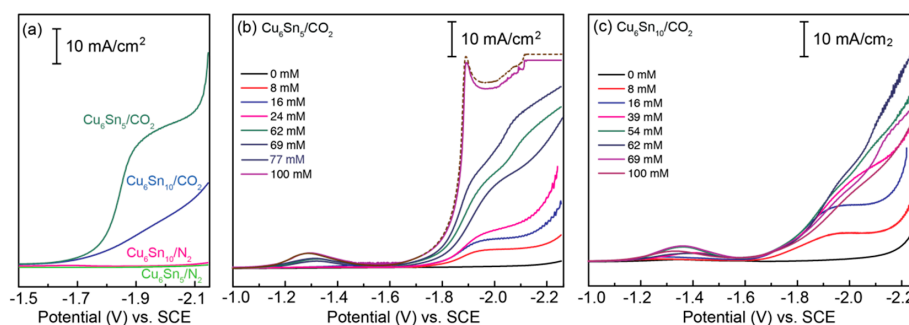


Figure 3. Linear sweep voltammograms (LSVs) recorded for (a) CuSn thin films in MeCN containing 0.1 M TBAPF₆ and 70 mM [BMIM]OTf under either CO₂ or N₂; (b) Cu₆Sn₅ in MeCN containing 0.1 M TBAPF₆ and varying concentrations of [BMIM]OTf under CO₂; (c) Cu₆Sn₁₀ in MeCN containing 0.1 M TBAPF₆ and varying concentrations of [BMIM]OTf under CO₂. Notably, no appreciable current response is observed for either CuSn alloy in the absence of CO₂ or [BMIM]OTf. All LSV data were recorded at a sweep rate of $\nu = 100$ mV/s. Note: LSVs recorded for Cu₆Sn₅ in the presence of more than 100 mM [BMIM]OTf do not change appreciably. A representative LSV obtained for Cu₆Sn₅ with more than 100 mM of [BMIM]OTf is represented by the dashed brown trace in panel (b).

Alteration of the Cu/Sn ratio of the thin-film catalysts impacts their activity toward CO₂ activation; for Cu₆Sn₅, the maximum current is reached at ~100 mM [BMIM]OTf, and that of Cu₆Sn₁₀ is reached at a concentration of ~60 mM (Figure 3). The CO₂RR current increases exponentially with the potential for Cu₆Sn₅, while for the electrode with excess Sn, the current increases linearly between –1.65 and –1.9 V, suggesting different limiting kinetics for the two systems, even at the relatively fast sweep rates ($\nu = 100$ mV/s) used to collect the voltammetry data shown in Figure 3.

Controlled potential electrolysis (CPE) of CO₂ saturated solutions of MeCN containing 0.1 M TBAPF₆ and [BMIM]OTf at –1.95 V versus SCE, were carried out for both the Cu₆Sn₅ and Cu₆Sn₁₀ cathodes. Table 1 summarizes how the CPE selectivities for the reduction of CO₂ to CO (FE_{CO}) are influenced by the amount of Sn in the alloys. The two alloys promote the evolution of CO with FE_{CO} = 34% and 41% for Cu₆Sn₅ and Cu₆Sn₁₀, respectively. In both cases, only minimal H₂ production is observed (FE_{H2} < 0.1%). The suppression of H₂ evolution observed for the CuSn alloys in the presence of [BMIM]⁺ is akin to that which has been observed for Bi and Sn cathodes in the presence of nonaqueous [Im]⁺-based electrolytes [16,20]. The proton equivalents needed for both the CO₂RR and H₂ evolution catalysis likely come from adventitious water in the MeCN-based electrolyte, and the weakly acidic [BMIM]⁺ cations (vide infra).

Table 1. Steady state Faradaic efficiencies (FE) and current density (j_{tot}) for controlled potential electrolysis at –1.95 V (SCE) using CuSn Alloys in MeCN-based electrolytes. Electrolysis experiments were conducted for 2.5 h. Table rows for experiments conducted in the absence of [BMIM]OTf are highlighted in blue.

Film	Electrolyte	FE _{CO}	FE _{H2}	j_{tot} (mA·cm ⁻²)
Cu ₆ Sn ₅	TBAPF ₆	41.1 ± 3.2%	4.4 ± 0.3%	0.44 ± 0.1
	TBAPF ₆ + [BMIM]OTf	34.4 ± 2.7%	<0.1%	3.9 ± 0.2
Cu ₆ Sn ₁₀	TBAPF ₆	22.5 ± 3.8%	3.9 ± 0.4%	0.6 ± 0.1
	TBAPF ₆ + [BMIM]OTf	30.5 ± 3.1%	<0.1%	2.8 ± 0.1

We have previously reported CPE with bare supporting Ni-electrodes in MeCN containing 0.1 M TBAPF₆ and [BMIM]OTf at –1.95 V versus SCE, and demonstrated that no CO₂RR takes place under these conditions [16,17]. Accordingly, the CO evolution reported in Table 1 must be promoted by the CuSn alloys. We note that the electrocatalytic formation of multicarbon products was not observed by NMR, consistent with prior studies of the CO₂RR on CuSn alloys under aqueous conditions [21]. The current densities for the CO₂RR are lower than those reported for electrodeposited non-noble metal cathodes such as Bi and Sn, which may be due to the electrodeposited platforms having much higher specific surface areas [16] compared with the evaporated CuSn films studied here. This difference in surface area (and therefore activity) is to be expected, as vapor depositions typically produce a smoother surface than those generated using electrodeposition methods. As such, we expect that CuSn alloys may demonstrate improved kinetics for the CO₂RR if synthesized through controlled co-electrodeposition methods or if used in nanoparticle form [25].

The formation of nonvolatile CO₂RR products was analyzed by ¹H NMR spectroscopy. Neither formate, formaldehyde, nor methanol, which are all common nonvolatile C₁ products formed from reduction of CO₂ were detected in the electrolyte solution following CPE experiments using either of the CuSn alloys as electrocatalysts. However, as shown in Figure 4, a product formed from the [BMIM]⁺ cation was observed by ¹H NMR. In particular, the analysis of the post electrolysis solution showed both distinct peaks for the starting [BMIM]⁺ cation as well as peaks corresponding to the zwitterionic [BMIM]–CO₂ adduct, as characterized by the diagnostic signals at 7.16 ppm in the ¹H NMR spectra [26–28]. The structure of the [BMIM]–CO₂ adduct is shown in Figure 5. We note that other than the starting [BMIM]⁺ and TBA⁺ cations, the [BMIM]–CO₂ adduct is the major solution-phase product following CPE and CO₂RR for both the C₆Sn₅ and C₆Sn₁₀ alloys, suggesting that the majority of the charge passed during the CPE experiments may be directed toward the activation of the [BMIM]⁺

as opposed to CO₂. Importantly, we note that this reactivity is distinct from that observed for Bi and Sn in MeCN-based electrolytes containing [Im]⁺-based cations [13,16,17].

The NMR spectra show that significantly less of the [BMIM]–CO₂ adduct is formed upon CPE with the Cu₆Sn₅ alloy compared with the analogous experiments employing the C₆Sn₁₀ thin film, as judged by the relative intensities of the adduct peaks at ~7.16 ppm versus those for the pristine [BMIM]⁺ cation at ~7.35 ppm, on both panels of Figure 4. We note that the position of the C(2)–H ¹H NMR resonance of [BMIM]⁺ varies between ~8.4–8.6 ppm for the two post-CPE spectra shown in Figure 5. This variance is likely due to hydrogen-bonding interactions between the anionic oxygen atoms of the electrochemically generated [BMIM]–CO₂ adduct and the acidic C(2)–H proton residue of [BMIM]⁺ in the solution [28]. Consistent with this rationale ([BMIM]–CO₂•••[BMIM]⁺) is the observation that the C(2)–H residue of [BMIM]⁺ appears further downfield (Figure 4, bottom) with increasing concentrations of the [BMIM]–CO₂ adduct. The formation of the [BMIM]–CO₂ adduct is undesirable because of its ability to bind strongly to acidic protons and catalyst surfaces [15,28]. As such, the observation (vide supra) that Cu₆Sn₁₀ displays a lower apparent rate order and current density for the CO₂RR is consistent with an enhanced production of [BMIM]–CO₂ with the more Sn-rich catalyst film.

3.3. Adsorption Pre-Catalysis Peak

There is a clear pre-catalysis wave in the LSV traces shown in Figure 3, centered around –1.4 V. Further inspection of the double layer regions by cyclic voltammetry (Figure 5) shows a clear quasi-reversible peak that is only observed in CO₂-saturated electrolyte solutions (Figure 5, right). The addition of 100 mM [BMIM]⁺ to the N₂-saturated MeCN containing 0.1 M TBAPF₆ (Figure 5, left) causes an increase of charge stored within the double layer region [29,30], which may be presumed to be due to the adsorption of [BMIM]⁺ at the electrode/electrolyte interface of the negatively polarized CuSn film [31–33]. Similar phenomena have been observed for Au electrodes [34–37], and it has been demonstrated that [Im]⁺ cations prefer to π -stack and lie flat on electrode surfaces, thereby supporting more capacitive charge build-up than an inner layer containing large TBA⁺ cations [38–40].

As shown in the right panel of Figure 5, the presence of [BMIM]⁺ appears to increase the cathodic (at –1.35 V) and anodic (at –0.90 V) waves associated with the precatalytic CO₂ binding wave. Imidazolium cations are known to coordinate strongly with CO₂ through π - π interactions, hydrogen bonding, and formation of CO₂ adducts [28]. As is also shown in the right panel of Figure 5 (black trace), a quasi-reversible wave is observed for CV traces recorded for the CuSn film in MeCN containing 0.1M TBAPF₆ under CO₂. This wave arises at potentials more positive than those required for CO₂RR catalysis, suggesting that the current response originates from the electrosorption of CO₂. The current response associated with this wave increases in the presence of 0.1 M [BMIM]⁺ (Figure 5, right, red trace), suggesting that [BMIM]⁺ is assisting in the CO₂ adsorption/activation, potentially via cooperative interactions between [BMIM]⁺, CO₂, and the negatively polarized CuSn film [17,41].

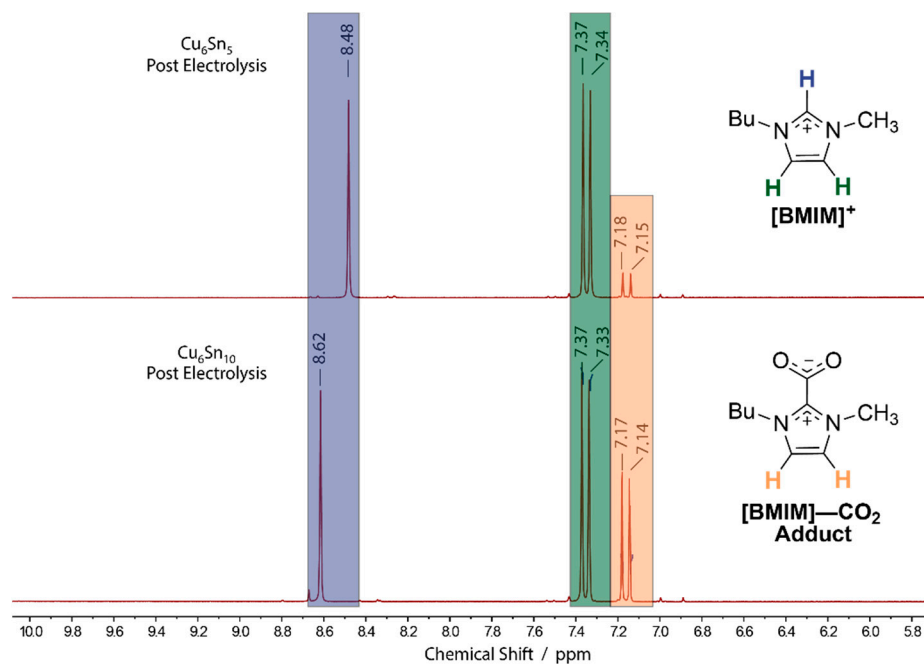


Figure 4. ^1H NMR of the electrolyte solutions following a 3-h controlled potential electrolysis (CPE) at -1.95 V (SCE) using either (**top**) Cu_6Sn_5 or (**bottom**) $\text{Cu}_6\text{Sn}_{10}$ cathodes. CPE experiments employed CO_2 -saturated MeCN solutions containing 0.1 M TBAPF $_6$ and $[\text{BMIM}]\text{OTf}$. Protonic resonances from the $[\text{BMIM}]^+$ and $[\text{BMIM}]-\text{CO}_2$ adduct are distinguished by color (blue, green, and orange).

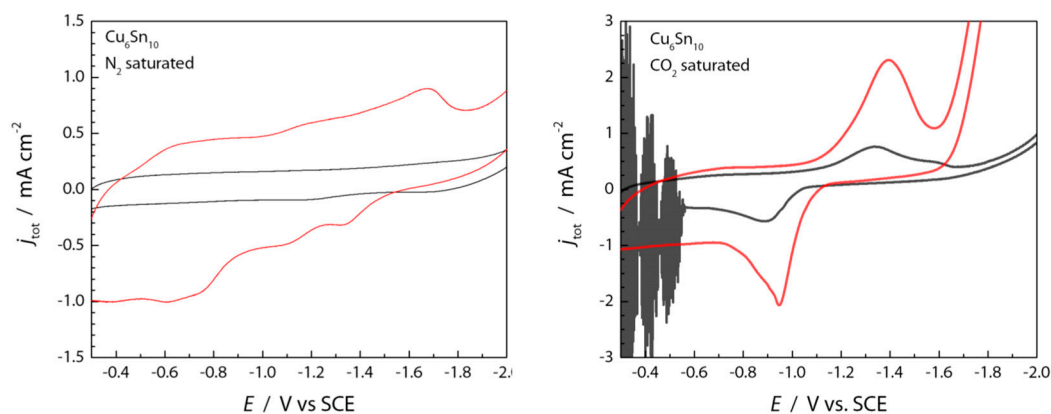


Figure 5. Cyclic voltammograms (CV) highlighting the electrochemical double layer region (N_2 sat) and the quasi-reversible pre-catalytic peak (CO_2 sat) with (red) and without (black) $[\text{BMIM}]\text{OTf}$ present. CV scans were initiated to negative potentials.

4. Conclusions

Electrochemical reduction of CO_2 to fuels using Cu-based cathodes and powered by renewable sources of electric current have attracted recent attention [42]. To date, however, CuSn alloys have been largely ignored as cathode materials for CO_2 reduction; however, these alloys are commonly available and inexpensive to produce, making them attractive material for the development of CO_2RR platforms. In this work, we have shown that sputtering CuSn thin film alloys produces submicron-sized particulates on Ni substrates. The CO_2RR activities of Cu_6Sn_5 and $\text{Cu}_6\text{Sn}_{10}$ films were ascertained by voltammetry and CPE experiments. When used in conjunction with imidazolium-based nonaqueous electrolytes, the CuSn films show activity for the reduction of CO_2 to CO at $E = -1.6$ V, and display modest Faradaic efficiencies for this transformation at an applied potential of $E = -1.95$ V. The CuSn alloy containing the higher ratio of Sn displayed lower efficiency and slower kinetics for the conversion of CO_2 to CO compared with Cu_6Sn_5 . CPE experiments conducted using both CuSn materials in the

presence of CO₂ and the [BMIM]⁺-containing electrolyte lead to deprotonation of the imidazolium and formation of the corresponding [BMIM]-CO₂ adduct, as judged by ¹H NMR experiments. Interestingly, the C₆Sn₁₀ material showed higher levels of [BMIM]-CO₂ generation, while displaying lower efficiency and activity for CO production, suggesting that the formation of the imidazolium-CO₂ adduct inhibits the CO₂RR with CuSn-based cathodes. We note that this deleterious reaction mode involving the [BMIM]⁺ electrolyte is not an issue for CuSn alloys employed for the CO₂RR with aqueous electrolytes that do not contain imidazolium cations. Accordingly, unlike other non-noble metal cathodes we have studied, CuSn alloys may be most useful for the CO₂RR when restricted to aqueous electrolyzer designs.

When both of the CuSn cathode materials are not utilized under aqueous conditions, the presence of the [BMIM]⁺ promoter in the CO-saturated MeCN-based electrolyte is critical to the observed CO₂RR activity. In addition to providing the proton equivalents required to drive the 2e⁻/2H⁺ conversion of CO₂ to CO, the [BMIM]⁺ ion also appears to promote the electrosorption of CO₂ at the CuSn/electrolyte interface, as judged by voltammetric experiments. As such, the interaction of the imidazolium electrolyte with the polarized CuSn cathodes and CO₂ is likely critical to improving the kinetics of the electrocatalysis, since the formation of surface-adsorbed CO₂ intermediates is energetically unfavorable and often rate-limiting for electrochemical CO₂RR platforms [41].

In future work, advanced spectroscopic methods will be useful tools as we seek to better understand the precise interplay between the adsorbed [Im]⁺ (and other electrolyte cations) and the cathode surface, and how the electrode/electrolyte interfacial structure affects CO₂ adsorption and reduction [39]. Recent work demonstrating that the interplay between adsorbed [Im]⁺ cations and other weakly acidic organic cations can be used to significantly enhance CO₂ reduction, as well as tune CO₂RR product distributions [17,29]. As such, further improvements in this aspect of the CO₂RR require the continued lowering of CO₂ adsorption/activation energy using electrolyte promoters, and the leveraging of [cation]⁺•••cathode interactions may be especially critical in this regard.

Author Contributions: The manuscript was written through contributions of all authors. All authors have given approval to the final version of the manuscript and contributed equally.

Funding: The experiments and authors were supported as part of the Fluid Interface Reactions, Structures and Transport (FIRST) Center, an Energy Frontier Research Center funded by the U.S. Department of Energy, Office of Science, Office of Basic Energy Sciences (BES-DOE).

Acknowledgments: The experiments and authors were supported as part of the Fluid Interface Reactions, Structures and Transport (FIRST) Center, an Energy Frontier Research Center funded by the U.S. Department of Energy, Office of Science, Office of Basic Energy Sciences (BES-DOE). This manuscript has been authored by UT-Battelle, LLC under Contract No. DE-AC05-00OR22725 with the U.S. Department of Energy. The United States Government retains and the publisher, by accepting the article for publication, acknowledges that the United States Government retains a non-exclusive, paid-up, irrevocable, world-wide license to publish or reproduce the published form of this manuscript, or allow others to do so, for United States Government purposes. The Department of Energy will provide public access to these results of federally sponsored research in accordance with the DOE Public Access Plan (<http://energy.gov/downloads/doe-public-access-plan>).

Conflicts of Interest: The authors declare no conflict of interest.

Abbreviations

[BMIM] ⁺	n-butyl-N'-methyl imidazolium
CPE	controlled potential electrolysis
DC	direct current
FE	Faradaic efficiency
GC	gas chromatography
NMR	nuclear magnetic resonance
TBA ⁺	tetrabutylammonium
OTf	triflate
SCE	standard calomel electrode
XPS	X-ray photoelectron spectroscopy

References

1. Lewis, N.S.; Nocera, D.G. Powering the planet: Chemical challenges in solar energy utilization. *Proc. Natl. Acad. Sci. USA* **2006**, *103*, 15729–15735. [[CrossRef](#)] [[PubMed](#)]
2. Cook, T.R.; Dogutan, D.K.; Reece, S.Y.; Surendranath, Y.; Teets, T.S.; Nocera, D.G. Solar energy supply and storage for the legacy and nonlegacy worlds. *Chem. Rev.* **2010**, *110*, 6474–6502. [[CrossRef](#)] [[PubMed](#)]
3. US Energy Information Administration. *Monthly Energy Review—May 2018*; U.S. Energy Information Administration: Washington, DC, USA, 2018.
4. Karl, T.R.; Trenberth, K.E. Modern global climate change. *Science* **2003**, *302*, 1719–1723. [[CrossRef](#)] [[PubMed](#)]
5. Olah, G.A.; Prakash, G.K.S.; Goepfert, A. Anthropogenic chemical carbon cycle for a sustainable future. *J. Am. Chem. Soc.* **2011**, *133*, 12881–12898. [[CrossRef](#)] [[PubMed](#)]
6. Aresta, M.; Dibenedetto, A.; Angelini, A. Catalysis for the valorization of exhaust carbon: From CO₂ to chemicals, materials, and fuels. technological use of CO₂. *Chem. Rev.* **2013**, *11*, 1709–1742. [[CrossRef](#)] [[PubMed](#)]
7. Lin, T.L.R.; Siang, Y.B. Recent advances in understanding mechanisms for the electrochemical reduction of carbon dioxide. *Curr. Opin. Electrochem.* **2018**, *8*, 126–134.
8. Rosenthal, J. *Progress Toward the Electrocatalytic Production of Liquid Fuels from Carbon Dioxide*; John Wiley & Sons, Inc.: Hoboken, NJ, USA, 2014; pp. 299–338.
9. Rosen, B.A.; Salehi-Khojin, A.; Thorson, M.R.; Zhu, W.; Whipple, D.T.; Kenis, P.J.A.; Masel, R.I. Ionic liquid-mediated selective conversion of CO₂ to CO at low overpotentials. *Science* **2011**, *334*, 643–644. [[CrossRef](#)] [[PubMed](#)]
10. Zhang, Z.; Chi, M.; Veith, G.M.; Zhang, P.; Lutterman, D.A.; Rosenthal, J.; Overbury, S.H.; Dai, S.; Zhu, H. Rational design of Bi nanoparticles for efficient electrochemical CO₂ Reduction: The elucidation of size and surface condition effects. *ACS Catal.* **2016**, *6*, 6255–6264. [[CrossRef](#)]
11. Sun, L.; Ramesha, G.K.; Kamat, P.V.; Brennecke, J.F. Switching the reaction course of electrochemical CO₂ reduction with ionic liquids. *Langmuir* **2014**, *30*, 6302–6308. [[CrossRef](#)]
12. Tanner, E.E.L.; Batchelor-Mcauley, C.; Compton, R.G. Carbon dioxide reduction in room-temperature ionic liquids: the effect of the choice of electrode material, cation, and anion. *J. Phys. Chem. C* **2016**, *120*, 26442–26447. [[CrossRef](#)]
13. Medina-Ramos, J.; DiMeglio, J.L.; Rosenthal, J. Efficient reduction of CO₂ To CO with high current density using in situ or ex situ prepared Bi-based materials. *J. Am. Chem. Soc.* **2014**, *136*, 8361–8367. [[CrossRef](#)] [[PubMed](#)]
14. Winikoff, S.G.; DiMeglio, J.L.; Chemburkar, A.; Medina-Ramos, J.; Rosenthal, J.; Neurock, M. Cooperativity between bismuth electrodes and ionic liquid electrolytes promotes efficient electrocatalytic reduction of CO₂ to CO. *Nat. Commun.* **2018**. submitted.
15. Matsubara, Y.; Grills, D.C.; Kuwahara, Y. Thermodynamic aspects of electrocatalytic CO₂ reduction in acetonitrile and with an ionic liquid as solvent or electrolyte. *ACS Catal.* **2015**, *5*, 6440–6452. [[CrossRef](#)]
16. Medina-Ramos, J.; Pupillo, R.C.; Keane, T.P.; DiMeglio, J.L.; Rosenthal, J. Efficient conversion of CO₂ to CO using tin and other inexpensive and easily prepared post-transition metal catalysts. *J. Am. Chem. Soc.* **2015**, *137*, 5021–5027. [[CrossRef](#)] [[PubMed](#)]
17. Atifi, A.; Boyce, D.W.; DiMeglio, J.L.; Rosenthal, J. Directing the outcome of CO₂ reduction at bismuth cathodes using varied ionic liquid promoters. *ACS Catal.* **2018**, *8*, 2857–2863. [[CrossRef](#)] [[PubMed](#)]
18. Furuya, N.; Motoo, S. The electrochemical behavior of ad-atoms and their effect on hydrogen evolution: Part I. Order-disorder rearrangement of copper ad-atoms on platinum. *J. Electroanal. Chem.* **1976**, *72*, 165–175. [[CrossRef](#)]
19. Furuya, N.; Motoo, S. The electrochemical behavior of ad-atoms and their effect on hydrogen evolution: Part IV. Tin and lead ad-atoms on platinum. *J. Electroanal. Chem.* **1979**, *98*, 195–202. [[CrossRef](#)]
20. DiMeglio, J.L.; Rosenthal, J. Selective conversion of CO₂ to CO with high efficiency using an inexpensive bismuth-based electrocatalyst. *J. Am. Chem. Soc.* **2013**, *135*, 8798–8801. [[CrossRef](#)]
21. Morimoto, M.; Takatsuji, Y.; Yamasaki, R.; Hashimoto, H.; Nakata, I.; Sakakura, T.; Haruyama, T. Electrodeposited Cu-Sn alloy for electrochemical CO₂ reduction to CO/HCOO⁻. *Electrocatalysis* **2018**, *9*, 323–332. [[CrossRef](#)]

22. Baggetto, L.; Jumas, J.-C.; Górká, J.; Bridges, C.A.; Veith, G.M. Predictions of particle size and lattice diffusion pathway requirements for sodium-ion anodes using H-Cu₆Sn₅ thin films as a model system. *Phys. Chem. Chem. Phys.* **2013**, *15*, 10885–10894. [[CrossRef](#)]
23. Moulder, J.F. *Handbook of X-ray Photoelectron Spectroscopy*; Physical Electronics: Eden Prairie, MN, USA, 1995.
24. Naille, S.; Dedryvère, R.; Martinez, H.; Leroy, S.; Lippens, P.E.; Jumas, J.C.; Gonbeau, D. XPS study of electrode/electrolyte interfaces of H-Cu₆Sn₅ electrodes in li-ion batteries. *J. Power Sources* **2007**, *174*, 1086–1090. [[CrossRef](#)]
25. Gawande, M.B.; Goswami, A.; Felpin, F.-X.; Asefa, T.; Huang, X.; Silva, R.; Zou, X.; Zboril, R.; Varma, R.S. Cu and Cu-based nanoparticles: Synthesis and applications in catalysis. *Chem. Rev.* **2016**, *116*, 3722–3811. [[CrossRef](#)] [[PubMed](#)]
26. Cabaço, M.I.; Besnard, M.; Chávez, F.V.; Pinaud, N.; Sebastião, P.J.; Coutinho, J.A.P.; Danten, Y. Understanding chemical reactions of CO₂ and its isoelectronic molecules with 1-butyl-3-methylimidazolium acetate by changing the nature of the cation: The case of CS₂ in 1-butyl-1-methylpyrrolidinium acetate studied by NMR spectroscopy and density functional theory calculations. *J. Chem. Phys.* **2014**, *140*, 244307. [[PubMed](#)]
27. Hanc-Scherer, F.A.; Montiel, M.A.; Montiel, V.; Herrero, E.; Sánchez-Sánchez, C.M. Surface structured platinum electrodes for the electrochemical reduction of carbon dioxide in imidazolium based ionic liquids. *Phys. Chem. Chem. Phys.* **2015**, *17*, 23909–23916. [[CrossRef](#)] [[PubMed](#)]
28. Scott, J.L.; Unali, G.; Perosa, A. A “By-productless” cellulose foaming agent for use in imidazolium ionic liquids. *Chem. Commun.* **2011**, *47*, 2970–2972. [[CrossRef](#)] [[PubMed](#)]
29. Zhang, Q.; Han, Y.; Wang, Y.; Ye, S.; Yan, T. Comparing the differential capacitance of two ionic liquid electrolytes: Effects of specific adsorption. *Electrochem. Commun.* **2014**, *38*, 44–46. [[CrossRef](#)]
30. Gore, T.R.; Bond, T.; Zhang, W.; Scott, R.W.J.; Burgess, I.J. Hysteresis in the measurement of double-layer capacitance at the gold–ionic liquid interface. *Electrochem. Commun.* **2010**, *12*, 1340–1343. [[CrossRef](#)]
31. Moganty, S.S.; Baltus, R.E.; Roy, D. Electrochemical windows and impedance characteristics of [Bmim+][] and [Bdmim+][] ionic liquids at the surfaces of Au, Pt, Ta and glassy carbon electrodes. *Chem. Phys. Lett.* **2009**, *483*, 90–94. [[CrossRef](#)]
32. Fedorov, M.V.; Kornyshev, A.A. Ionic liquids at electrified interfaces. *Chem. Rev.* **2014**, *114*, 2978–3036. [[CrossRef](#)]
33. Kirchner, K.; Kirchner, T.; Ivaništšev, V.; Fedorov, M.V. Electrical double layer in ionic liquids: Structural transitions from multilayer to monolayer structure at the interface. *Electrochim. Acta* **2013**, *110*, 762–771. [[CrossRef](#)]
34. Black, J.M.; Walters, D.; Labuda, A.; Feng, G.; Hillesheim, P.C.; Dai, S.; Cummings, P.T.; Kalinin, S.V.; Proksch, R.; Balke, N. Bias-dependent molecular-level structure of electrical double layer in ionic liquid on graphite. *Nano Lett.* **2013**, *13*, 5954–5960. [[CrossRef](#)] [[PubMed](#)]
35. Uysal, A.; Zhou, H.; Feng, G.; Lee, S.S.; Li, S.; Cummings, P.T.; Fulvio, P.F.; Dai, S.; McDonough, J.K.; Gogotsi, Y.; et al. Interfacial ionic “liquids”: Connecting static and dynamic structures. *J. Phys. Condens. Matter* **2014**, *27*. [[CrossRef](#)] [[PubMed](#)]
36. Lauw, Y.; Horne, M.D.; Rodopoulos, T.; Lockett, V.; Akgun, B.; Hamilton, W.A.; Nelson, A.R.J. Structure of [C 4mpyr][NTf 2] room-temperature ionic liquid at charged gold interfaces. *Langmuir* **2012**, *28*, 7374–7381. [[CrossRef](#)] [[PubMed](#)]
37. García Rey, N.; Dlott, D.D. Structural transition in an ionic liquid controls CO₂ electrochemical reduction. *J. Phys. Chem. C* **2015**, *119*, 20892–20899. [[CrossRef](#)]
38. Siinor, L.; Siimenson, C.; Ivaništšev, V.; Lust, K.; Lust, E. Influence of cation chemical composition and structure on the double layer capacitance for Bi(111)/room temperature ionic liquid interface. *J. Electroanal. Chem.* **2012**, *668*, 30–36. [[CrossRef](#)]
39. Yanson, A.I.; Rodriguez, P.; Garcia-Araez, N.; Mom, R.V.; Tichelaar, F.D.; Koper, M.T.M. Cathodic corrosion: A quick, clean, and versatile method for the synthesis of metallic nanoparticles. *Angew. Chem. Int. Ed.* **2011**, *50*, 6346–6350. [[CrossRef](#)]
40. Hersbach, T.J.P.; Yanson, A.I.; Koper, M.T.M. Anisotropic etching of platinum electrodes at the onset of cathodic corrosion. *Nat. Commun.* **2016**, *7*, 1–7. [[CrossRef](#)]

41. Tian, Z.; Priest, C.; Chen, L. Recent progress in the theoretical investigation of electrocatalytic reduction of CO₂. *Adv. Theory Simul.* **2018**, *1*, 1800004–1800023. [[CrossRef](#)]
42. Kunene, T.; Xiong, L.; Rosenthal, J. Solar-powered synthesis of hydrocarbons from carbon dioxide and water. *Proc. Natl. Acad. Sci. USA* **2019**, *116*, 9693–9695. [[CrossRef](#)]



© 2019 by the authors. Licensee MDPI, Basel, Switzerland. This article is an open access article distributed under the terms and conditions of the Creative Commons Attribution (CC BY) license (<http://creativecommons.org/licenses/by/4.0/>).